The soft discrete element method

Guilhem Mollon

The soft discrete element method

Guilhem Mollon[1]

Abstract
In order to accelerate simulations of assemblies of highly deformable grains, a novel numerical approach, called Soft Discrete Element Method (SDEM) is presented. It consists in extending the classical DEM by introducing the deformability of the grains in a simplified way. Simple kinematics are postulated in order to represent the ovalisation of the grains and their local deformations around interparticle contacts. Adequate equations of motion are derived, and a contact model is proposed in the framework of elastic frictionless grains. Comparisons are made with existing analytical and numerical solutions, and the ability of this method to simulate the compressibility and some micromechanical aspects of this class of materials is validated. Upon implementation in optimized DEM codes, the SDEM is expected to allow large scale simulations of samples of deformable particles.

Keywords Granular media · Discrete modelling · Soft grains · SDEM

1 Introduction

The Discrete Element Method (DEM, [1]) has now become ubiquitous in the field of granular science, because it offers a large number of advantages when compared to a continuous modelling of granular samples: it is conceptually simple, versatile, and particularly informative about local quantities that may be out of reach for experimentalists. Modern refinements of this technique (e.g. use of complex/realistic grain shapes [2–4], enrichment of contact laws [5, 6], coupling with different physics [7, 8], etc.) allow it to deal with a broad range of scientific and technological applications. A major assumption of DEM, however, is the perfect rigidity of the grains (only slightly degraded by the small interpenetrations allowed at the contacts). This assumption is sensible in most applications, but becomes very questionable when the level of stress applied to the sample is of the same order of magnitude as the stiffness of the material composing the grains. If this material is ductile enough (i.e. if grain breakage is disregarded), such a situation should lead to large deformations of the grains (Fig. 1), which is prevented in the strict framework of DEM.

✉ Guilhem Mollon
guilhem.mollon@insa-lyon.fr

[1] Université de Lyon, LaMCoS, INSA-Lyon, CNRS UMR5259, 69621 Lyon, France

Several numerical approaches have been proposed to deal with highly deformable grains [9–12], and all of them rely on some sort of discretization of the grains. This is notably the case of the Multibody Meshfree Approach [13, 14], which was implemented in the open source code MELODY [15]. In this framework, a large number of field nodes are positioned in each grain and on its contour. Each field node carries two degrees of freedom in displacement, and the displacement field is interpolated between the nodes using meshfree shape functions. This choice was made to improve the robustness of the code when grains are submitted to very large deformations. Grains contours are represented by a piecewise-linear frontier, and contacts are treated by a robust two-pass node-to-segment algorithm. This technique was successfully applied in granular physics [16], tribology [17, 18], geomechanics [4], and geophysics [19].

A major limitation of this tool, however, is its computational cost. The large number of degrees of freedom and the small time steps typically limit this approach to samples of a few thousands grains at the most, while classical DEM can nowadays deal with several millions of them. To go beyond this limitation, this paper presents a novel approach for the simulation of large samples of soft grains. This approach, called the Soft Discrete Element Method (SDEM), is based on a different philosophy inspired both by the field of Model Order Reduction [20–22] and by Moveable Cellular Automatons [23, 24]. It consists in simplifying

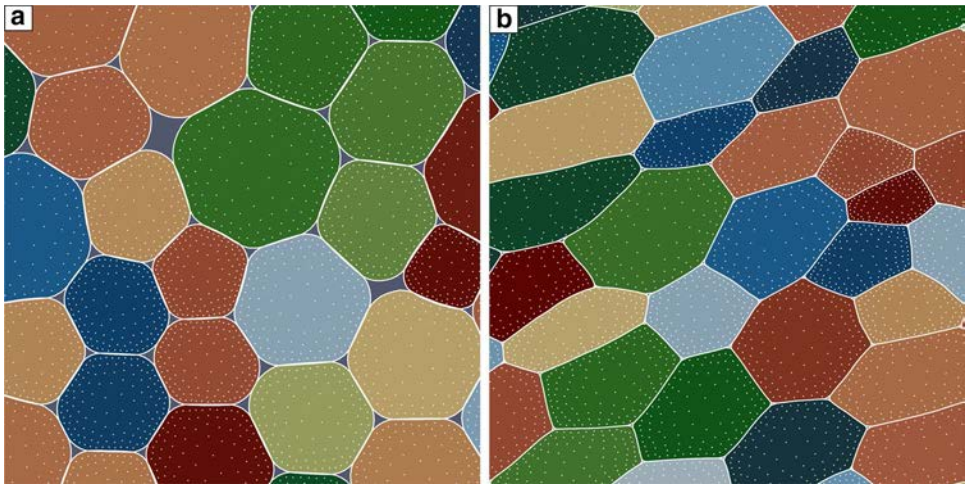

Fig. 1 Close views on numerical experiments performed on soft grains with the Multibody Meshfree Approach; **a** Frictionless isotropic compaction; **b** Isochoric deviatoric loading at maximum compaction with friction

considerably the kinematics of the soft grains by only considering a very limited number of deformation modes. It leads to a dramatic reduction in the computational cost, but keeps the main physics at work in samples of highly deformable grains. Section 2 of this paper presents these simplified kinematics, and Section 3 develops the associated equations of motions. In Section 4, the stress tensor and the contact forces are derived, as well as the techniques associated with the numerical solver. Section 5 proposes a validation of the method by comparing it with existing analytical and numerical solutions.

2 Kinematics

2.1 Degrees of freedom

We first define the main frame $\{O, \overrightarrow{e_X}, \overrightarrow{e_Y}\}$ of the problem, which remains fixed. For a given grain, an attached rigid-body motion frame is defined as $\{C, \overrightarrow{e_x}, \overrightarrow{e_y}\}$, with C being its center of mass. In the proposed numerical framework a 2D deformable grain is assumed to have only six degrees of freedom. Three of them are related to rigid-body motions: two translations of the grain center of mass $x_c(t)$ and $y_c(t)$ (which define the position of C with respect to O) and one rotation $\theta(t)$ (which is the angle of the direction $\overrightarrow{e_x}$ with respect to $\overrightarrow{e_X}$). The remaining three degrees of freedom are related to the deformations of the grain: they are the two principal strains $\varepsilon_1(t)$ and $\varepsilon_2(t)$ (with no specific ordering) and the angle $\alpha(t)$ of orientation of the principal deformation frame $\{C, \overrightarrow{e_1}, \overrightarrow{e_2}\}$ with respect to the rigid-body frame $\{C, \overrightarrow{e_x}, \overrightarrow{e_y}\}$ attached to the grain. Namely, $\alpha(t)$ is the angle between the direction $\overrightarrow{e_x}$ and the direction $\overrightarrow{e_1}$ of the main stretching $\varepsilon_1(t)$. This is summarized in Fig. 2, for a grain with an initial radius $R = 0.5$. $\varepsilon_1(t)$, $\varepsilon_2(t)$ and $\alpha(t)$ actually define a strain tensor, which is assumed to be constant over the whole domain covered by the grain:

$$\overline{\overline{\varepsilon}} = \begin{bmatrix} \varepsilon_1 & 0 \\ 0 & \varepsilon_2 \end{bmatrix}_{\{\overrightarrow{e_1},\overrightarrow{e_2}\}} = \begin{bmatrix} \varepsilon_{xx} & \varepsilon_{xy} \\ \varepsilon_{xy} & \varepsilon_{yy} \end{bmatrix}_{\{\overrightarrow{e_x},\overrightarrow{e_y}\}} = \begin{bmatrix} \varepsilon_{XX} & \varepsilon_{XY} \\ \varepsilon_{XY} & \varepsilon_{YY} \end{bmatrix}_{\{\overrightarrow{e_X},\overrightarrow{e_Y}\}} \tag{1}$$

When submitted to such a homogeneous strain field, a circular grain will take the shape of an ellipse with two orthogonal half-axes of respective lengths $R \cdot \big(1 + \varepsilon_1(t)\big)$ and $R \cdot \big(1 + \varepsilon_2(t)\big)$, oriented along the frame $\{C, \overrightarrow{e_1}, \overrightarrow{e_2}\}$.

These kinematics are thus more complex that those commonly encountered in 2D DEM, as they offer the possibility for each grain to gain a certain amount of ellipticity as a response to the loads it is submitted to. This is, obviously, a strong simplification of the real kinematics of deformable grains which, to be represented in detail, would require a much larger number of degrees of freedom (using for example shape functions attached to field nodes, like in the multibody meshfree approach, [13, 14]). As we demonstrate in the remainder of this paper, it provides nevertheless a satisfactory description of the main physics of assemblies of deformable grains.

The main question that arises is: how to determine the evolution in time of these six degrees of freedom? Newtonian dynamics can be readily applied to the three components of the rigid body motion (accounting for the possible changes in rotational inertia brought by the deformations), but the case of the three other degrees of freedom is less straightforward. The usual way to predict the deformation of a solid is to employ a constitutive model, i.e. a relation (usually based on thermodynamics and phenomenological observations) between the stress tensor and the strain tensor. Since the strain is assumed to be homogeneous in the grain, so must be the stress. We thus define a homogeneous field of stress tensor within a given grain as follows:

$$\overline{\overline{\sigma}} = \begin{bmatrix} \sigma_1 & 0 \\ 0 & \sigma_2 \end{bmatrix}_{\{\overrightarrow{e_1},\overrightarrow{e_2}\}} = \begin{bmatrix} \sigma_{xx} & \sigma_{xy} \\ \sigma_{xy} & \sigma_{yy} \end{bmatrix}_{\{\overrightarrow{e_x},\overrightarrow{e_y}\}} = \begin{bmatrix} \sigma_{XX} & \sigma_{XY} \\ \sigma_{XY} & \sigma_{YY} \end{bmatrix}_{\{\overrightarrow{e_X},\overrightarrow{e_Y}\}} \tag{2}$$

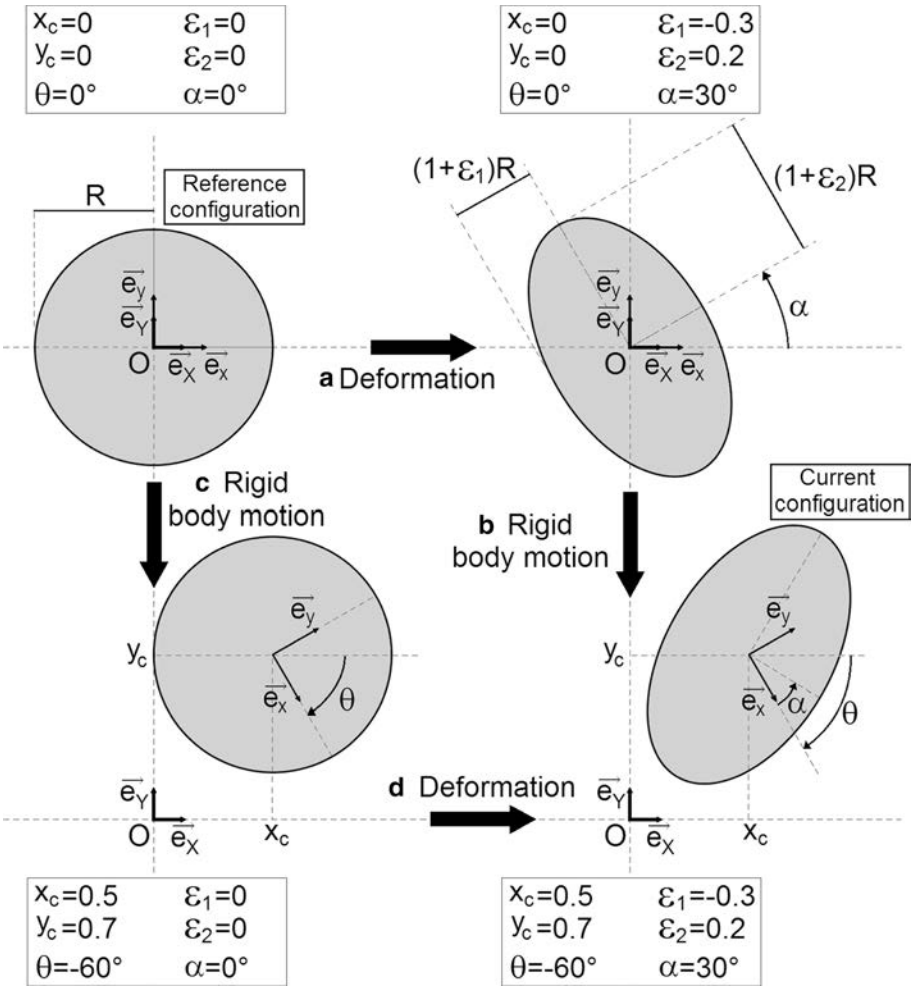

Fig. 2 Illustration of the six degrees of freedom for an initially circular grain. The path to the current configuration can be conceptualized either by a deformation (**a**) followed by a rigid body motion (**b**), or by a rigid body motion (**c**) followed by a deformation (**d**)

The principal directions of this stress tensor are aligned with those of the strain tensor if the chosen constitutive model is isotropic, which is postulated in the remainder of this paper for the sake of simplicity.

A given grain is submitted to a number of external forces applied on its external contour. These forces can be summarized, as is often done in granular science, by an equivalent stress field called $\overline{\overline{\sigma}}_{ext}$. If static equilibrium is reached, the resulting force and torque applied to the grain are null and the stress within the grain $\overline{\overline{\sigma}}$ is equal to that induced by the external forces $\overline{\overline{\sigma}}_{ext}$. However, DEM simulations are dynamic by nature, and so is the proposed method. Hence, static equilibrium is never perfectly enforced. There is always some amount of unbalanced force and, in the present case, of unbalanced stress. Such a system hence relies on equations of motion, which have to be written for each degree of freedom. Any such equation must establish a relation between a generalized force and a generalized mass (both associated to a given degree of freedom) on one hand, and the second time-derivative of the concerned degree of freedom, on the other hand. The six equations of motion are derived in Section 3 for the postulated kinematics.

2.2 Deformations around contacts

The general ovalisation of the grain shape captures well some features of the grains deformation shown in Fig. 1, but a major element is still missing. It is, indeed, impossible with such kinematics to represent properly the closure of the intergranular space under a sufficiently large confining stress. The missing ingredient is the local deformation of the grains in the direct neighbourhood of their contacts. We clearly observe in Fig. 1 that, if the grains are squeezed enough, they do not exhibit any more a point contact like in usual rigid granular materials. Instead of this, the matter around the contact deforms to accommodate the load, and the contact point becomes a contact area (or contact line in 2D). As the load increases, these contact lines occupy a larger proportion of the grains contours, until the whole contour of each grain is in contact with other grains and the porosity is closed. We also observe in Fig. 1 that, at least

in the case where the constitutive model is the same for all grains, the contact line between any two grains is never far from a linear segment.

In classical DEM, a small interpenetration is allowed between contacting grains, in order to compute a repulsive force opposing to contact. In most cases, the normal stiffness used to compute this force is seen as a numerical parameter of regularization rather than as a physical quantity. In some contexts (e.g. small strain behaviours of sands), this interpenetration is seen as a proxy for the local contact-induced deformation. The classical Hertz theory ([25]) can for example be applied to compute the repulsive normal force between two spheres on physical grounds, and the Hertz–Mindlin model ([26]) can be applied the same way to derive both normal and tangential components of this force. These approaches, however, rely on rather restrictive assumptions, including the necessity for the deformation (and thus for the interpenetration) to remain small with respect to the grain size. For this reason, they cannot be directly applied in the present context.

Precisely describing the large deformation of the matter composing the grains in the neighbourhood of a heavily loaded contact would require a much larger number of degrees of freedom than the six that were defined in the previous section, and would contradict the general spirit of the method. Alternatively, we propose here to account for this phenomenon in a simplified way. We accept that very large interpenetrations take place between the ellipses representing the contacting grains, but we then assume that the real contours of the grains in that case are not completely represented by the ellipses. In the contact area, the contour is replaced by a straight segment linking the two intersection points between the ellipses, as represented in Fig. 3. Hence, in the case of multiple contacts, a given

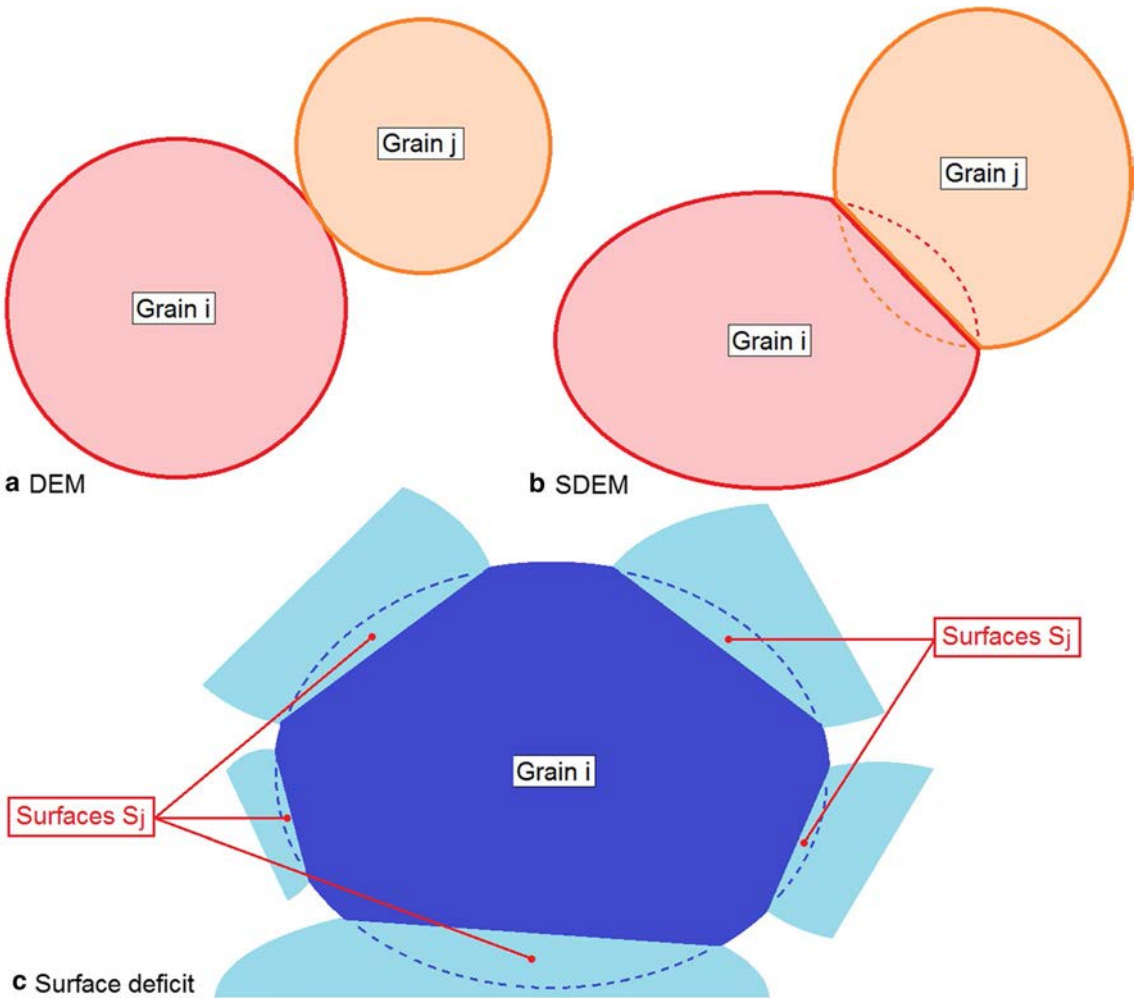

Fig. 3 **a**, **b** Difference in contact conceptualization between DEM (rigid discs with "point" contact represented by a very limited interpenetration) and SDEM (deformed grains with large deformations around the contact area, represented by a local contact segment); **c** Illustration of the surface deficit $\sum_j S_j$ for grain i induced by interpenetrations with its neighbors

grain contour is a succession of straight segments and of portions of the main ellipse defined by the kinematics of the previous section.

Obviously, this assumption means that a large part of the grains surface areas (i.e. all the area of each ellipse located beyond the contact segment) is ignored, which could be seen as a problem in terms of conservation laws. A simple solution exists to solve this issue: since this loss of surface can be computed, it can be added to the strain tensor as a spherical (i.e. purely volumetric) term, and thus be accounted for when applying the constitutive model to compute the stress tensor. If we assume, for example, that the material composing the grains is incompressible (i.e. any loss of surface is prohibited), then the surface area lost beyond the contact segment will be regained by an increase of ε_1 and ε_2 in accordance with the chosen constitutive model. This approach is detailed in Section 4, as well as the calibration of the contact forces associated with such a contact segment.

3 Equations of motion

3.1 Degrees of freedom of the rigid-body part of the motion:

In this paragraph, we consider that a grain with an initial radius R and a unit mass ρ has acquired a certain deformation (defined by the degrees of freedom ε_1, ε_2, and α), and that it is subjected to a rigid-body motion while keeping a constant shape. The case of the translational degrees of freedom x_c and y_c is straightforward, as they obey to the classical Newtonian laws of dynamics, written as:

$$\begin{cases} \ddot{x}_c(t) = \frac{F_x(t)}{M_x} \\ \ddot{y}_c(t) = \frac{F_y(t)}{M_y} \end{cases} \tag{3}$$

where $F_x(t)$ and $F_y(t)$ are the resulting forces applied on the grain and:

$$M_x = M_y = \rho\pi R^2 \tag{4}$$

The case of the rotational rigid motion is just less straightforward, since it requires to account for the current shape of the grain. It writes:

$$\ddot{\theta}(t) = \frac{C_\theta(t)}{M_\theta(t)} \tag{5}$$

where $C_\theta(t)$ is the resulting torque applied on the grain, and $M_\theta(t)$ is the current rotational inertia of the deformed elliptic grain (Fig. 4a):

$$M_\theta(t) = \left(1+\varepsilon_1(t)\right)^2 \cdot \left(1+\varepsilon_2(t)\right)^2 \cdot \frac{\rho\pi R^4}{2} \tag{6}$$

3.2 Degrees of freedom ε_1 and ε_2

In this paragraph and the next one, we consider that the degrees of freedom related to the rigid motion of the grains (i.e. x_c, y_c, and θ) are kept constant and equal to zero. We thus only consider a deformation of the grain defined by two principal strains ε_1 and ε_2, oriented along an angle α. Under these assumptions, a point of position (X, Y) in the reference configuration is located at a certain time t at the location $(x(t), y(t))$ given by:

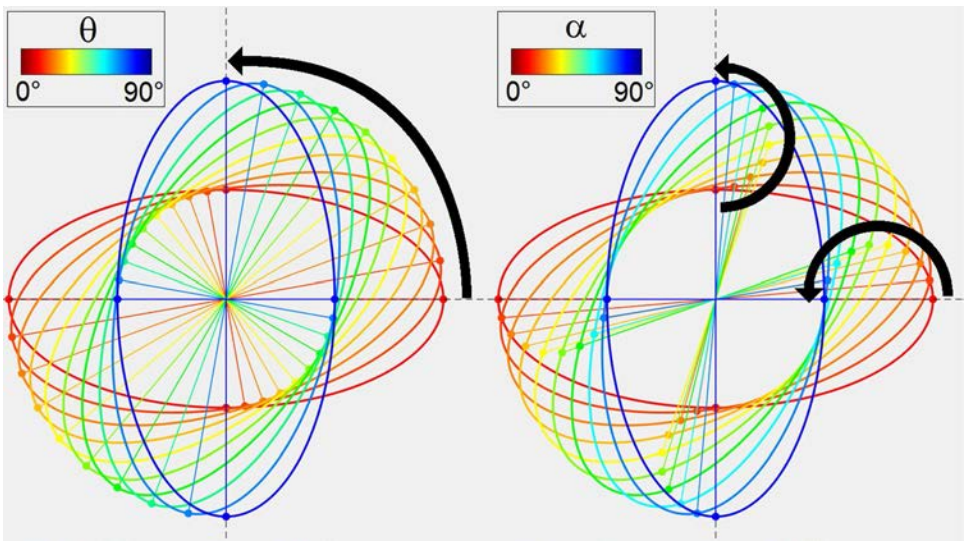

Fig. 4 Differences between the degrees of freedom θ (rigid-body rotation) and α (change in the orientation of the principle directions of strain) for $\varepsilon_1 = 1$ and $\varepsilon_2 = 0$. Note in particular the motion of a given material point when each degree of freedom is continuously increased from 0° to 90° (black arrows)

$$\begin{cases} x(t) = \left(1+\varepsilon_1(t)\right)\cdot\left(X\cdot\cos^2\alpha(t) + Y\cdot\cos\alpha(t)\cdot\sin\alpha(t)\right) + \left(1+\varepsilon_2(t)\right)\cdot\left(X\cdot\sin^2\alpha(t) - Y\cdot\cos\alpha(t)\cdot\sin\alpha(t)\right) \\ y(t) = \left(1+\varepsilon_1(t)\right)\cdot\left(X\cdot\cos\alpha(t)\cdot\sin\alpha(t) + Y\cdot\sin^2\alpha(t)\cdot\sin\alpha(t)\right) + \left(1+\varepsilon_2(t)\right)\cdot\left(-X\cdot\cos\alpha(t)\cdot\sin\alpha(t) + Y\cdot\cos^2\alpha(t)\right) \end{cases} \tag{7}$$

We first consider that ε_2 and α are constant in time, and we compute the velocity of this point as a function of $\varepsilon_1(t)$:

$$\begin{cases} \dot{x}(t) = \dot{\varepsilon}_1(t)\cdot\left(X\cdot\cos^2\alpha + Y\cdot\cos\alpha\cdot\sin\alpha\right) \\ \dot{y}(t) = \dot{\varepsilon}_1(t)\cdot\left(X\cdot\cos\alpha\cdot\sin\alpha + Y\cdot\sin^2\alpha\right) \end{cases} \tag{8}$$

If we assign a mass dm to every such material point, the total kinetic energy corresponding at a certain time t to the variation of $\varepsilon_1(t)$ is thus given by:

$$E_{c1}(t) = \int_\Omega \frac{\dot{x}^2(t)+\dot{y}^2(t)}{2}dm \tag{9}$$

where Ω is, for example, the geometric domain occupied by the body in its reference configuration. Thus, in polar coordinates (r,θ), we have $X = r\cdot\cos\theta$ and $Y = r\cdot\sin\theta$, giving:

$$\begin{aligned} &E_{c1}(t) \\ &= \int_0^{2\pi}\int_0^R \left[\dot{\varepsilon}_1^2(t)\cdot\frac{\left(r\cdot\cos\theta\cdot\cos^2\alpha + r\cdot\sin\theta\cdot\cos\alpha\cdot\sin\alpha\right)^2}{2}\right. \\ &\left.+\dot{\varepsilon}_1^2(t)\cdot\frac{\left(r\cdot\cos\theta\cdot\cos\alpha\cdot\sin\alpha + r\cdot\sin\theta\cdot\sin^2\alpha\right)^2}{2}\right]\rho\cdot r\cdot drd\theta \end{aligned} \tag{10}$$

This energy can be reorganized under the form:

$$E_{c1}(t) = \frac{1}{2}M_1\cdot\dot{\varepsilon}_1^2(t) \tag{11}$$

where M_1 is the generalized mass associated with the degree of freedom ε_1, and given by:

$$M_1 = \rho\cdot\int_0^{2\pi}\int_0^R \left[\left(r\cdot\cos\theta\cdot\cos^2\alpha + r\cdot\sin\theta\cdot\cos\alpha\cdot\sin\alpha\right)^2 + \left(r\cdot\cos\theta\cdot\cos\alpha\cdot\sin\alpha + r\cdot\sin\theta\cdot\sin^2\alpha\right)^2\right]\cdot r\cdot drd\theta \tag{12}$$

Which yields:

$$M_1 = \rho\cdot\int_0^{2\pi}\int_0^R r^3\cdot\cos^2(\theta-\alpha)\cdot drd\theta \tag{13}$$

And finally:

$$M_1 = \rho\pi R^4/4 \tag{14}$$

In order to compute the generalized force associated with the same degree of freedom, we postulate that there exists an unbalanced homogeneous stress field $\overline{\overline{s}}(t)$ in the body at a certain time t:

$$\overline{\overline{s}}(t) = \begin{bmatrix} s_{XX}(t) & s_{XY}(t) \\ s_{XY}(t) & s_{YY}(t) \end{bmatrix}_{\{\vec{e_X},\vec{e_Y}\}} = \begin{bmatrix} s_{11}(t) & s_{12}(t) \\ s_{12}(t) & s_{22}(t) \end{bmatrix}_{\{\vec{e_1},\vec{e_2}\}} \tag{15}$$

This unbalanced stress corresponds to the stress $\overline{\overline{\sigma}}_{ext}(t)$ induced by external forces applied on the grain, corrected by the stress $\overline{\overline{\sigma}}(t)$ related to the current strain tensor of the body by the means of a given constitutive model (see section 4). Since this field is homogeneous in the grain, there is an associated resulting force field in each material point of initial coordinates (X,Y):

$$\begin{cases} F_x(X,Y,t) = -\frac{s_{XX}(t)}{X} - \frac{s_{XY}(t)}{Y} \\ F_y(X,Y,t) = -\frac{s_{YY}(t)}{Y} - \frac{s_{XY}(t)}{X} \end{cases} \tag{16}$$

Hence, the generalized force associated with the degree of freedom ε_1 is given by the general expression:

$$F_1(t) = \int_\Omega \left(\frac{\partial x}{\partial\varepsilon_1}(X,Y,t)\cdot F_x(X,Y,t) + \frac{\partial y}{\partial\varepsilon_1}(X,Y,t)\cdot F_y(X,Y,t)\right)d\Omega \tag{17}$$

where $(x(t),y(t))$ are the current coordinates of the point of reference coordinates (X,Y). Still considering ε_2 and α as constant in time, and using Eq. (7), we have:

$$\begin{cases} \frac{\partial x}{\partial\varepsilon_1}(X,Y,t) = X\cdot\cos^2\alpha + Y\cdot\cos\alpha\cdot\sin\alpha \\ \frac{\partial y}{\partial\varepsilon_1}(X,Y,t) = X\cdot\cos\alpha\cdot\sin\alpha + Y\cdot\sin^2\alpha \end{cases} \tag{18}$$

These expressions are then injected in $F_1(t)$ from Eq. (17):

$$F_1(t) = -\int_\Omega \left(\left(X\cdot\cos^2\alpha + Y\cdot\cos\alpha\cdot\sin\alpha\right)\cdot\left(\frac{s_{XX}(t)}{X} + \frac{s_{XY}(t)}{Y}\right) + \left(X\cdot\cos\alpha\cdot\sin\alpha + Y\cdot\sin^2\alpha\right)\cdot\left(\frac{s_{YY}(t)}{Y} + \frac{s_{XY}(t)}{X}\right)\right)d\Omega \tag{19}$$

If the grain is considered as isotropic, the generalized force of the degree of freedom ε_1 (related to the extension/compression in the direction $\overrightarrow{e_1}$) should be independent from the value of the angle α, and we can thus choose $\alpha = 0$. In that case, the frames $\left\{O, \overrightarrow{e_x}, \overrightarrow{e_y}\right\}$ and $\left\{O, \overrightarrow{e_1}, \overrightarrow{e_2}\right\}$ are identical, and we can rewrite the generalized force:

$$F_1(t) = -\int_\Omega X \cdot \left(\frac{s_{11}(t)}{X} + \frac{s_{12}(t)}{Y}\right) d\Omega \tag{20}$$

Integrating this simple expression on the reference domain finally leads to:

$$F_1(t) = -\pi R^2 \cdot s_{11}(t) \tag{21}$$

This result provides the generalized expression for the dynamics of the degree of freedom ε_1:

$$\ddot{\varepsilon}_1(t) = \frac{F_1(t)}{M_1} \tag{22}$$

Similar expressions are derived for ε_2. We have:

$$\ddot{\varepsilon}_2(t) = \frac{F_2(t)}{M_2} \tag{23}$$

with $M_2 = M_1$ and:

$$F_2(t) = -\pi R^2 \cdot s_{22}(t) \tag{24}$$

3.3 Degree of freedom α

We now consider that ε_1 and ε_2 are constant in time (Fig. 4b), and we derive the new expressions for the current velocity of a given point of initial coordinates (X, Y) and of current coordinates $(x(t), y(t))$. For that purpose, we differentiate in time the Eq. (7):

$$\begin{cases} \dot{x}(t) = -2\left(1+\varepsilon_1\right)X \cdot \sin\alpha(t) \cdot \cos\alpha(t) \cdot \dot{\alpha}(t) + 2\left(1+\varepsilon_2\right)X \cdot \sin\alpha(t) \cdot \cos\alpha(t) \cdot \dot{\alpha}(t) + Y\left(\varepsilon_1 - \varepsilon_2\right) \cdot \left(\cos^2\alpha(t) - \sin^2\alpha(t)\right) \cdot \dot{\alpha}(t) \\ \dot{y}(t) = -2\left(1+\varepsilon_2\right)Y \cdot \sin\alpha(t) \cdot \cos\alpha(t) \cdot \dot{\alpha}(t) + 2\left(1+\varepsilon_1\right)Y \cdot \sin\alpha(t) \cdot \cos\alpha(t) \cdot \dot{\alpha}(t) + X\left(\varepsilon_1 - \varepsilon_2\right) \cdot \left(\cos^2\alpha(t) - \sin^2\alpha(t)\right) \cdot \dot{\alpha}(t) \end{cases} \tag{25}$$

This expression simplifies to:

$$\begin{cases} \dot{x}(t) = \dot{\alpha}(t) \cdot \left(\varepsilon_1 - \varepsilon_2\right) \cdot \left(-X \cdot \sin^2\alpha(t) + Y \cdot \cos^2\alpha(t)\right) \\ \dot{y}(t) = \dot{\alpha}(t) \cdot \left(\varepsilon_1 - \varepsilon_2\right) \cdot \left(Y \cdot \sin^2\alpha(t) + X \cdot \cos^2\alpha(t)\right) \end{cases} \tag{26}$$

The kinetic energy associated with this degree of freedom is thus equal to:

$$E_{c\alpha}(t) = \int_\Omega \frac{\dot{x}^2(t) + \dot{y}^2(t)}{2} dm \tag{27}$$

As in the previous paragraph, this energy can be reorganized under the form:

$$E_{c\alpha}(t) = \frac{1}{2} M_\alpha(t) \cdot \dot{\alpha}^2(t) \tag{28}$$

where $M_\alpha(t)$ is the generalized mass associated with this degree of freedom, and given by:

$$M_\alpha(t) = \int_\Omega \left[\left(\varepsilon_1 - \varepsilon_2\right)^2 \cdot \left(-X \cdot \sin^2\alpha(t) + Y \cdot \cos^2\alpha(t)\right)^2 + \left(\varepsilon_1 - \varepsilon_2\right)^2 \cdot \left(Y \cdot \sin^2\alpha(t) + X \cdot \cos^2\alpha(t)\right)^2\right] dm \tag{29}$$

This expression simplifies to:

$$M_\alpha(t) = \left(\varepsilon_1 - \varepsilon_2\right)^2 \int_\Omega \left(X^2 + Y^2\right) dm \tag{30}$$

After a simple integration on the reference domain, the generalized mass is:

$$M_\alpha(t) = \left(\varepsilon_1(t) - \varepsilon_2(t)\right)^2 \frac{\rho\pi R^4}{2} \tag{31}$$

It is interesting to observe that this mass is not constant in time, since it depends on the values of ε_1 and ε_2 (it vanishes if the grain is circular, i.e. if $\varepsilon_1 = \varepsilon_2$, since the grain cannot deform along the degree of freedom α in that particular case). When implemented numerically, M_α will thus have to be updated at each time step.

To compute the corresponding generalized force, we use a formula analogous to Eq. (17):

$$F_\alpha(t) = \int_\Omega \left(\frac{\partial x}{\partial \alpha}(X, Y, t) \cdot F_x(X, Y, t) + \frac{\partial y}{\partial \alpha}(X, Y, t) \cdot F_y(X, Y, t)\right) d\Omega \tag{32}$$

where the force field is given in Eq. (16). The partial derivatives are computed from Eq. (7) and give, at the end of the calculation:

$$\begin{cases} \frac{\partial x}{\partial \alpha}(X,Y,t) = \left(\varepsilon_1 - \varepsilon_2\right) \cdot \left(-X \cdot \sin^2 \alpha(t) + Y \cos^2 \alpha(t)\right) \\ \frac{\partial y}{\partial \alpha}(X,Y,t) = \left(\varepsilon_1 - \varepsilon_2\right) \cdot \left(Y \cdot \sin^2 \alpha(t) + X \cos^2 \alpha(t)\right) \end{cases} \tag{33}$$

Injecting them and the force field in Eq. (32) yields:

$$\begin{aligned} F_\alpha(t) = -\int_\Omega & \left(\left(\varepsilon_1 - \varepsilon_2\right) \cdot \left(-X \cdot \sin^2 \alpha(t) + Y \cos^2 \alpha(t)\right)\right. \\ & \cdot \left(\frac{s_{XX}(t)}{X} + \frac{s_{XY}(t)}{Y}\right) + \left(\varepsilon_1 - \varepsilon_2\right) \\ & \left.\cdot \left(Y \cdot \sin^2 \alpha(t) + X \cos^2 \alpha(t)\right) \cdot \left(\frac{s_{YY}(t)}{Y} + \frac{s_{XY}(t)}{X}\right)\right) d\Omega \end{aligned} \tag{34}$$

For reasons similar to those used in the previous paragraph, this generalized force should be independent on the value of the angle α (i.e. it should be frame-independent to remain objective), and we can use an arbitrary value for this parameter, such as $\alpha = 0$:

$$F_\alpha(t) = -\left(\varepsilon_1 - \varepsilon_2\right) \int_\Omega \left(Y \cdot \left(\frac{s_{11}(t)}{X} + \frac{s_{12}(t)}{Y}\right) + X \cdot \left(\frac{s_{22}(t)}{Y} + \frac{s_{12}(t)}{X}\right)\right) d\Omega \tag{35}$$

After integration, we finally obtain:

$$F_\alpha(t) = -2\pi R^2 \cdot \left(\varepsilon_1(t) - \varepsilon_2(t)\right) \cdot s_{12}(t) \tag{36}$$

Just like the generalized mass, this force vanishes for a circular shape (i.e. $\varepsilon_1 = \varepsilon_2$). The general expression of the time-dynamics of the degree of freedom α is thus:

$$\ddot{\alpha}(t) = \frac{F_\alpha(t)}{M_\alpha(t)} \tag{37}$$

3.4 Summary

Based on the calculations derived in the previous paragraph, we can summarize the equations of motion of a given grain of initial radius R and of initial unit mass ρ:

$$\begin{cases} \ddot{x}_c(t) = \frac{F_x(t)}{\rho\pi R^2} \\ \ddot{y}_c(t) = \frac{F_y(t)}{\rho\pi R^2} \\ \ddot{\theta}(t) = \frac{2 \cdot C_\theta(t)}{\left(1+\varepsilon_1(t)\right)^2 \cdot \left(1+\varepsilon_2(t)\right)^2 \cdot \rho\pi R^4} \end{cases} \quad \text{and} \quad \begin{cases} \ddot{\varepsilon}_1(t) = -\frac{4 \cdot s_{11}(t)}{\rho R^2} \\ \ddot{\varepsilon}_2(t) = -\frac{4 \cdot s_{22}(t)}{\rho R^2} \\ \ddot{\alpha}(t) = -\frac{4 \cdot s_{12}(t)}{\left(\varepsilon_1(t) - \varepsilon_2(t)\right)\rho R^2} \end{cases} \tag{38}$$

Using these equations of motion requires to compute both the external forces applied on the grain and its internal stress field.

4 Forces and stresses

4.1 Stress tensors

As exposed in the previous sections, two stress tensors need to be defined. The first one, noted $\overline{\overline{\sigma}}$, is related in a univocal way to the strain tensor by the means of the constitutive model, and thus represents the actual stress in the grain. The second one, noted $\overline{\overline{\sigma}}_{ext}$, serves as a compact reduction of the internal efforts induced in the grain by all the contact forces applied on its contour. As a first step into this novel technique, very simple assumptions are to be made. We assume in this paper that a linear relationship exists between the stress and strain tensors. Since we wish to account for the surface loss at the contact segments between grains, we need to distinguish the volumetric and deviatoric parts of the strain tensor. The deviatoric part is:

$$\varepsilon_{1dev}(t) = \varepsilon_1(t) - \left(\varepsilon_1(t) + \varepsilon_2(t)\right)/2 \tag{39}$$

$$\varepsilon_{2dev}(t) = \varepsilon_2(t) - \left(\varepsilon_1(t) + \varepsilon_2(t)\right)/2 \tag{40}$$

The volumetric part accounts both for the surface change related to the main deformations ε_1 and ε_2, and for the surface losses S_j related to the intersection of the corresponding grain with any other contacting grain j (Fig. 3c):

$$\varepsilon_V(t) = \frac{\pi R^2 \cdot \left(1 + \varepsilon_1(t)\right)\left(1 + \varepsilon_2(t)\right) - \sum_j S_j}{\pi R^2} - 1 \tag{41}$$

It should be noted that this evaluation of the volumetric strain does not rely on the trace of $\overline{\overline{\varepsilon}}$, since this approach would only be licit in the limit of small strains. In the more general case of finite strains, which is more likely to be encountered in the present situation, it is necessary to compute directly the area of the deformed grain based on the lengths of its main axes. With this decomposition, we can thus deduce the following stress field:

$$\sigma_1(t) = (2\mu + \lambda) \cdot \varepsilon_{1dev}(t) + \lambda \cdot \varepsilon_{2dev}(t) + \kappa \cdot \varepsilon_V(t) \tag{42}$$

$$\sigma_2(t) = \lambda \cdot \varepsilon_{1dev}(t) + (2\mu + \lambda) \cdot \varepsilon_{2dev}(t) + \kappa \cdot \varepsilon_V(t) \tag{43}$$

where μ and λ are the Lamé coefficients and κ is the bulk modulus, related to Young's modulus and Poisson's coefficient by:

$$\lambda = \frac{E\nu}{(1+\nu)(1-2\nu)} \tag{44}$$

$$\mu = \frac{E}{2(1+\nu)} \tag{45}$$

$$\kappa = \frac{E}{(3-6\nu)} \tag{46}$$

Hence, equations of linearized elasticity are applied even though finite strains are expected in the system. Future extensions of the method might include more complex constitutive relations, such as hyper-elasticity or elasto-plasticity.

The external stress tensor associated to the contact forces applied on a given grain is given by the classical Love–Weber formula ([27]):

$$\left(\overline{\overline{\sigma}}_{ext}\right)_{ij} = \frac{1}{S}\sum_{contacts} F_i \cdot r_j \tag{47}$$

where S is the particle surface area, F_i are the components of the force $\overrightarrow{F_c}$ associated to a given contact, and r_j are the components of the corresponding branch vector (i.e. the vector linking the grain center of mass and a representative contact point). When both $\overline{\overline{\sigma}}$ and $\overline{\overline{\sigma}}_{ext}$ are determined, the unbalanced stress to be used in the equations of motion of the previous section is simply given by:

$$\overline{\overline{s}}(t) = \overline{\overline{\sigma}}_{ext}(t) - \overline{\overline{\sigma}}(t) \tag{48}$$

4.2 Contact algorithm and contact law

Applying Eq. (47) requires the computation of contact forces between two grains (and possibly between a single grain and a boundary wall). This force should depend on the local contact conditions (based on quantities such as interpenetration distance, etc.) and on the constitutive behavior of the contacting grains. A contact algorithm is therefore necessary. Several algorithms were proposed in the literature to characterize the intersection between arbitrary ellipses [28–30]. Since they were proposed in a classical DEM framework, they were optimized for the case of small interpenetrations,

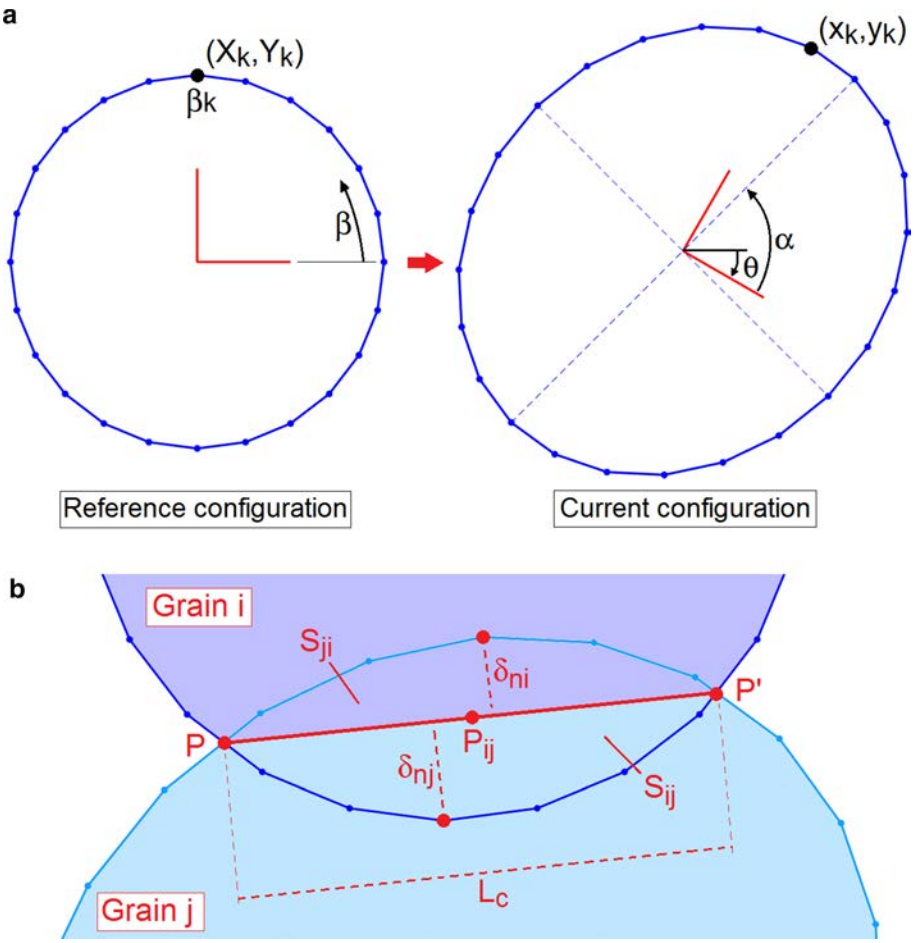

Fig. 5 **a** Change of coordinates from the reference to the current configuration $(\theta = -30°,\ \alpha = 75°,\ \varepsilon_1 = 0.3,\ \varepsilon_1 = 0.1)$; **b** Local contact quantities computed based on piecewise-linear contours

and relied on the fact that the shape and size of the ellipses were considered as constant.

In order to bring more generality to the method and to its future extensions, the first implementation of SDEM that is presented here is based on a discretization of the contour of each ellipse, with an angular parameterization of the reference (circular and un-rotated) shape of each grain (Fig. 5). For a given grain i of initial radius R_i, a number of nodes N_n is positioned on the contour of reference, parameterized by the angle $\beta_k = [0, \delta\beta, 2\delta\beta, \ldots, 2\pi - \delta\beta]$ with an angular step $\delta\beta = 2\pi/N_n$ (a value of $\delta\beta = 1°$ is used in the present work). At a given time in a simulation, if the degrees of freedom of the grains i take the values $\{x_{ci}, y_{ci}, \theta_i, \varepsilon_{1i}, \varepsilon_{2i}, \alpha_i\}$, the coordinates of these contour nodes become:

$$\begin{bmatrix} x_{ki} \\ y_{ki} \end{bmatrix} = A \cdot \begin{bmatrix} X_{ki} \\ Y_{ki} \end{bmatrix} + B \tag{49}$$

With the reference coordinates:

$$\begin{cases} X_{ki} = R_i \cdot \cos\beta_k \\ Y_{ki} = R_i \cdot \sin\beta_k \end{cases} \tag{50}$$

And with:

$$B = \begin{bmatrix} x_{ci} \\ y_{ci} \end{bmatrix} \tag{51}$$

$$A = \begin{bmatrix} a_{11} & a_{12} \\ a_{21} & a_{22} \end{bmatrix} \tag{52}$$

$$\begin{cases} a_{11} = \left(\varepsilon_1 \cos^2 a + \varepsilon_2 \sin^2 a + 1\right)\cos\theta - \left(\varepsilon_1 - \varepsilon_2\right)\cos\alpha \sin\alpha \sin\theta \\ a_{12} = \left(\varepsilon_1 - \varepsilon_2\right)\cos\alpha \sin\alpha \cos\theta - \left(\varepsilon_1 \sin^2\alpha + \varepsilon_2 \cos^2\alpha + 1\right)\sin\theta \\ a_{21} = \left(\varepsilon_1 \cos^2 a + \varepsilon_2 \sin^2 a + 1\right)\sin\theta + \left(\varepsilon_1 - \varepsilon_2\right)\cos\alpha \sin\alpha \cos\theta \\ a_{22} = \left(\varepsilon_1 - \varepsilon_2\right)\cos\alpha \sin\alpha \sin\theta + \left(\varepsilon_1 \sin^2\alpha + \varepsilon_2 \cos^2\alpha + 1\right)\cos\theta \end{cases} \tag{53}$$

The transformation defined by Eq. (49) allows for a rapid evaluation of the current coordinates of each node on the contour of the grains. A simple intersection algorithm based on a piecewise linear approximation of the current contour of each grain is then applied. For any pair of contacting grains i and j, this allows for a rapid computation of key quantities such as the normal gaps δ_{ni} and δ_{nj} (taken as negative is there is an interpenetration of the grains), the interpenetration areas S_{ij} and S_{ji}, and the two intersection points P and P'. The contact length L_c is then taken as the distance PP', defining a tangential vector $\vec{t} = \overrightarrow{PP'}/L_c$ and its associated normal vector (Fig. 5). A representative point of contact P_{ij} is also defined as the mid-point between P and P', and used as the point of application of the contact force (in particular for the computation of C_θ and $\overline{\overline{\sigma}}_{ext}$). Similar calculations are done for contacts between a grain and an infinite boundary wall.

At that point, it is necessary to establish a relation between the local contact parameters and the contact force. In classical DEM, the standard contact model relies on the concept of contact stiffness, which is usually seen as a numerical regularization of the non-penetration condition. Since it does not bear any physical meaning (except in a limited number of situations, e.g. [31, 32]), its value is determined in order to ensure limited interpenetrations under the expected average normal load on each contact. In SDEM, however, the non-penetration condition is not enforced, since large overlaps between the deformed grains are expected. Besides, the contact force is seen in this framework as the result of local deformations of the grains, and should therefore be related in some way to their constitutive models. While the Hertzian model is licit at small interpenetrations, its general assumptions are too restrictive to be applied to the present case, especially because of the large deformations of the grains around the contacts. In the general case, it is expected that no closed-form solution can be found for this force, but a simple heuristic model can be proposed under the present assumptions (elastic grains, no friction, no cohesion). We postulate that the contact-related deformation of the grain remains local, and is limited to an area defined by (i) the contact segment and (ii) a curve which is defined as

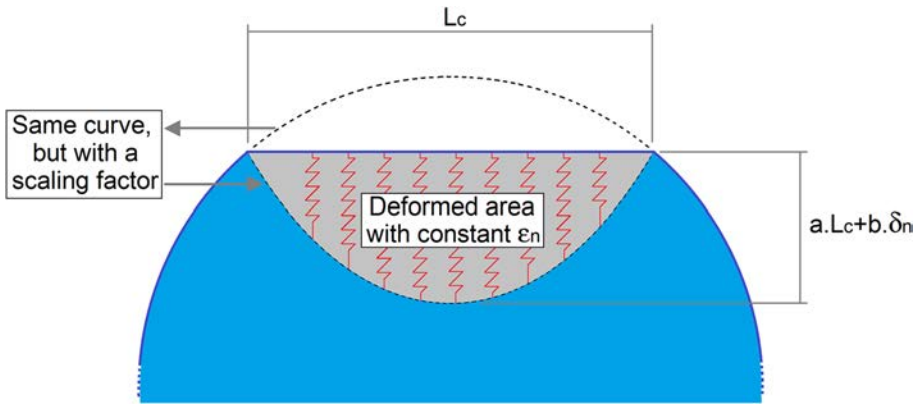

Fig. 6 Sketch of the proposed contact model

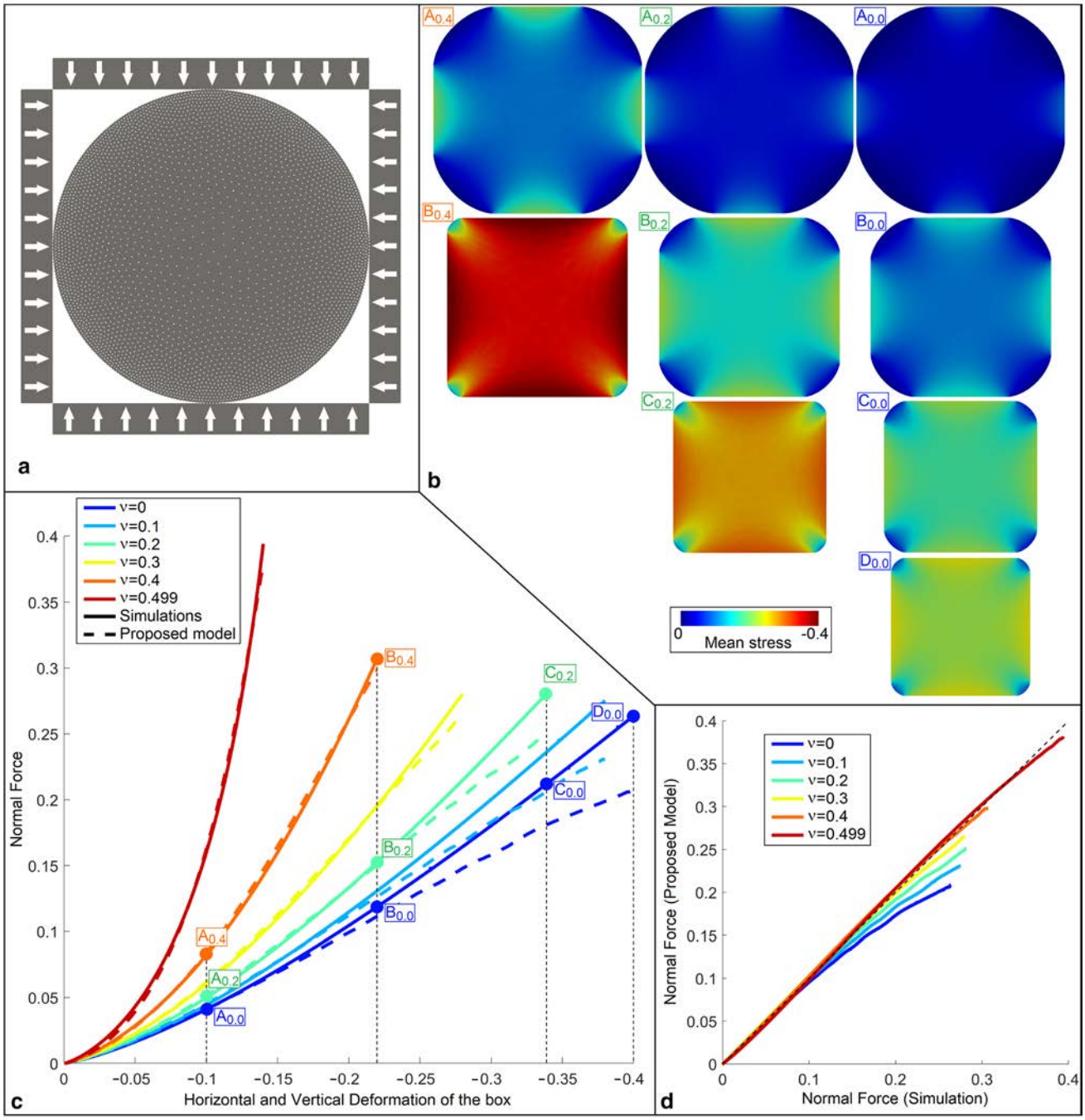

Fig. 7 Calibration of the contact model; **a** Simulation of single grain isotropic compression; **b** Fields of mean stress in the grain at different compression stages and for Poisson Coefficients of 0.4, 0.2, and 0 (from left to right); **c** Normal force in each grain-wall contact as a function of the deformation of the box, provided by the simulations and by the proposed contact model with a = 0.58 and b = 2; **d** Direct comparison between the forces provided by the simulations and by the proposed contact model

the symmetrical curve to the initial contour of the grain (i.e. as it would be in the absence of contact) but with a certain scaling factor (Fig. 6). The exact expression of these curves (which are portions of ellipses) does not need to be known. In this area, the deformation is postulated to be constant, and to occur only in the direction normal to the contact. It is thus called ε_n. We also define the normal gap δ_n as the average between the gaps computed for the two grains concerned with the contact:

$$\delta_n = \frac{\delta_{ni} + \delta_{nj}}{2} < 0 \tag{54}$$

We then assume that the maximum dimension of the deformed area in the normal direction is a linear composition of the two characteristic dimensions of the contact, namely its length L_c and its normal gap δ_n. With these assumptions, the normal strain ε_n in the deformed area is related to the ratio between the initial dimensions of the deformed area (in the direction normal to the contact) to its current dimensions.

Considering the point of maximum interpenetration (Fig. 6), we can write:

$$\varepsilon_n = \frac{\delta_n}{\left(a \cdot L_c + b \cdot \delta_n\right) - \delta_n} \tag{55}$$

Considering linear elasticity and integrating the normal stress on the whole contact length, we finally get a repulsive normal force equal to:

$$F_n = E \cdot \varepsilon_n \cdot L_c = k_n \cdot \delta_n \tag{56}$$

With a secant normal stiffness k_n given by:

$$k_n = \frac{E \cdot L_c}{a \cdot L_c + (b-1) \cdot \delta_n} \tag{57}$$

where a and b are two constants. It is interesting to notice that this expression is independent on the grain radius. To determine a and b, numerical simulations of the isotropic compression of a deformable grain between four walls are performed with the code MELODY [15]. The grain has a diameter equal to 1 and a unit Young modulus, and several values of the Poisson Coefficient (ranging between 0 and 0.5) are tested. This process is summarized in Fig. 7a. As observed in Fig. 7b, the grain shape flattens at the contact, but the stress level remains rather constant on the contact segment, as postulated in the proposed contact model. At each time of each simulation, it is thus possible to measure the value of L_c and to compute the value of δ_n (by considering the virtual circle that crosses the square box at the extremities of the contact segments). For given values of a and b, it is thus possible to apply the Eqs. (56–57) and to compare the obtained force with that provided by the simulation. This is done in Fig. 7c with $a = 0.58$ and $b = 2$ (i.e. with the same parameters for all values of the Poisson coefficient). The agreement is fairly good, except for low Poisson Coefficients (i.e. $\nu < 0.2$) at very large compressive strains, where the model underestimates the normal contact force by up to 15% (Fig. 7d). Additional tests performed with different values of the radius and of the Young modulus (not reported here) confirmed this agreement. This is quite remarkable because the proposed contact model is very simplistic and relies on assumptions which are obviously wrong. It nevertheless offers a simple way to estimate the repulsive force between deformable grains with large interpenetration, at a very small computational cost.

4.3 Solver, stability, damping, and incompressibility

In order to integrate in time the equations of motion summarized in Eq. (38), a time step Δt is chosen, and an explicit solver is employed in the same manner as classical DEM. Considering for example the degree of freedom x_c, we apply at each time step the following algorithm:

$$\dot{x}_c \leftarrow \dot{x}_c + \Delta t \cdot \frac{F_x(t)}{M_x} \tag{58}$$

$$x_c \leftarrow x_c + \Delta t \cdot \dot{x}_c \tag{59}$$

Analogous formulations are used for the five other degrees of freedom. Since this solver is explicit, the question of its stability is essential. A critical point is the degree of freedom α, because its associated generalized mass M_α, provided in Eq. (29), depends on the current state of deformation of the grain. More importantly, in the circular state of reference of each grain, this generalized mass vanishes to 0. It means that, for very small (in absolute value) levels of deformation $\varepsilon_1 - \varepsilon_2$, this mass is extremely small, and requires a very small time step. This is clearly a waste of computational resources, since the parameter α has only a very small influence on the grain shape when the deviatoric deformation is low. A simple way to bypass this limitation is to ignore the generalized force F_α is the mass M_α is too small compared to the generalized mass of the other deformation-related degrees of freedom. Hence, at each time step and for each grain, the following condition is checked:

$$M_\alpha > k_\alpha \cdot M_{\varepsilon 1} \tag{60}$$

where k_α is a user-defined constant. If this condition is not verified, the force F_α receives the value 0 before applying Eqs. (58–59), which prevents any instability. Typical values of k_α of the order of 10^{-3} seem to provide satisfactory results. An alternative approach is to apply a constant mass scaling to M_α (i.e. to multiply it by a factor 100, for example), but it is only licit in quasi-static situations (i.e. when the dynamic response of this degree of freedom is unimportant), and it does not solve the singular case $M_\alpha = 0$ (when $\varepsilon_1 = \varepsilon_2$, for example in the initial circular state). In the illustrative simulations described in the next section, a combination of both techniques was implemented.

Another condition to ensure stability is to introduce a certain amount of damping to dissipate kinetic energy. In classical DEM this is introduced in the contact law, and this

approach is reproduced in the present study. We thus add to each contact force a damping term with the expression:

$$F_{damp} = -\gamma \cdot \sqrt{\frac{k_n}{\frac{1}{M_i} + \frac{1}{M_j}}} \cdot \dot{\delta}_n \tag{61}$$

where γ is a damping coefficient, k_n is the secant contact stiffness provided in Eq. (57), M_i and M_j are the masses of the two grains into contact, and $\dot{\delta}_n$ is the time-derivative of the normal gap (computed by numerical derivation based on the previous time step). In addition, we must apply a damping on the degrees of freedom involving a deformation of the grains (i.e. ε_1, ε_2, and α) in order to attenuate their free oscillations in the absence of contact. Hence, we add the following terms to the generalized forces of ε_1, ε_2, and α respectively (Eqs. (21) and (36)):

$$F_{1,damp} = -\gamma \cdot M_1 \cdot \dot{\varepsilon}_1 \tag{62}$$

$$F_{2,damp} = -\gamma \cdot M_2 \cdot \dot{\varepsilon}_2 \tag{63}$$

$$F_{\alpha,damp} = -\gamma \cdot M_\alpha \cdot \dot{\alpha} \tag{64}$$

For quasi-static simulations, a value $\gamma = 1$ proved satisfactory.

In many practical and academic situations, soft grains are considered as incompressible (or at least, their compressibility is negligible compared to their deformability). This is problematic, because incompressibility is notoriously difficult to introduce in simulated elastic media (may it be in a discrete or in a continuous framework), due to the divergence of the bulk modulus towards infinity. A common solution for this issue is to introduce a Poisson coefficient close to—but not equal to—0.5. Typical values could be 0.49, 0.499, etc. This is analogous to a numerical penalization of any shift from perfect incompressibility. This solution is convenient but presents two drawbacks: incompressibility is only enforced in an imperfect way, and it strongly reduces the critical time step of explicit solvers (because the bulk modulus, although not infinite, is very high). In the SDEM framework introduced here, this drawback can be circumvented by applying a simple technique. It consists in applying a Poisson coefficient strictly equal to 0.5, but in computing the internal stress field based only on the deviatoric part of the strain tensor. Hence, Eqs. (42–43) are replaced by:

$$\sigma_1(t) = 2\mu \cdot \varepsilon_{1dev}(t) \tag{65}$$

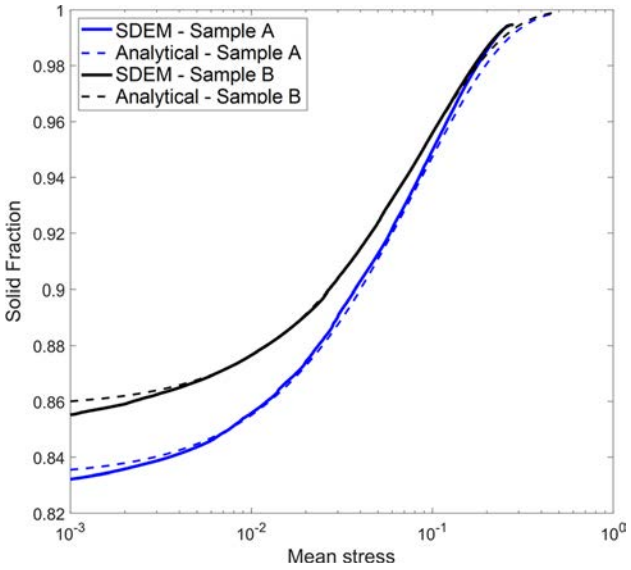

Fig. 8 Comparison with the analytical solution of [33] for incompressible grains

$$\sigma_2(t) = 2\mu \cdot \varepsilon_{2dev}(t) \tag{66}$$

This avoids any problem related to the singularity of κ. To enforce incompressibility, though, it is necessary to keep the volume of the grains constant. Hence, after updating the deformation of the grain in Eqs. (58–59) based on the stress tensor of Eqs. (65–66), an additional isotropic deformation should be added to the grain. The added volumetric strain ε_{Vadd} should verify (for a given grain i in contact with several grains j):

$$\pi R^2 \left(1 + \varepsilon_{1dev} + \frac{\varepsilon_{Vadd}}{2}\right)\left(1 + \varepsilon_{2dev} + \frac{\varepsilon_{Vadd}}{2}\right) - \sum_j S_j = \pi R^2 \tag{67}$$

Which yields:

$$\varepsilon_{Vadd} = -\varepsilon_{1dev} - \varepsilon_{2dev} - 2 + \sqrt{\left(\varepsilon_{1dev} + \varepsilon_{2dev} + 2\right)^2 - 4\left(\left(1 + \varepsilon_{1dev}\right)\left(1 + \varepsilon_{2dev}\right) - 1 - \frac{\sum_j S_j}{\pi R^2}\right)} \tag{68}$$

We then simply add $\varepsilon_{Vadd}/2$ to ε_{1dev} and ε_{2dev} before starting a new time step.

5 Validation

5.1 Isotropic compression

In order to check that the proposed method offers a satisfactory representation of the mechanical response of collections of deformable grains, we first consider the isotropic compaction of two samples of ~ 1000 grains. The sample A follows

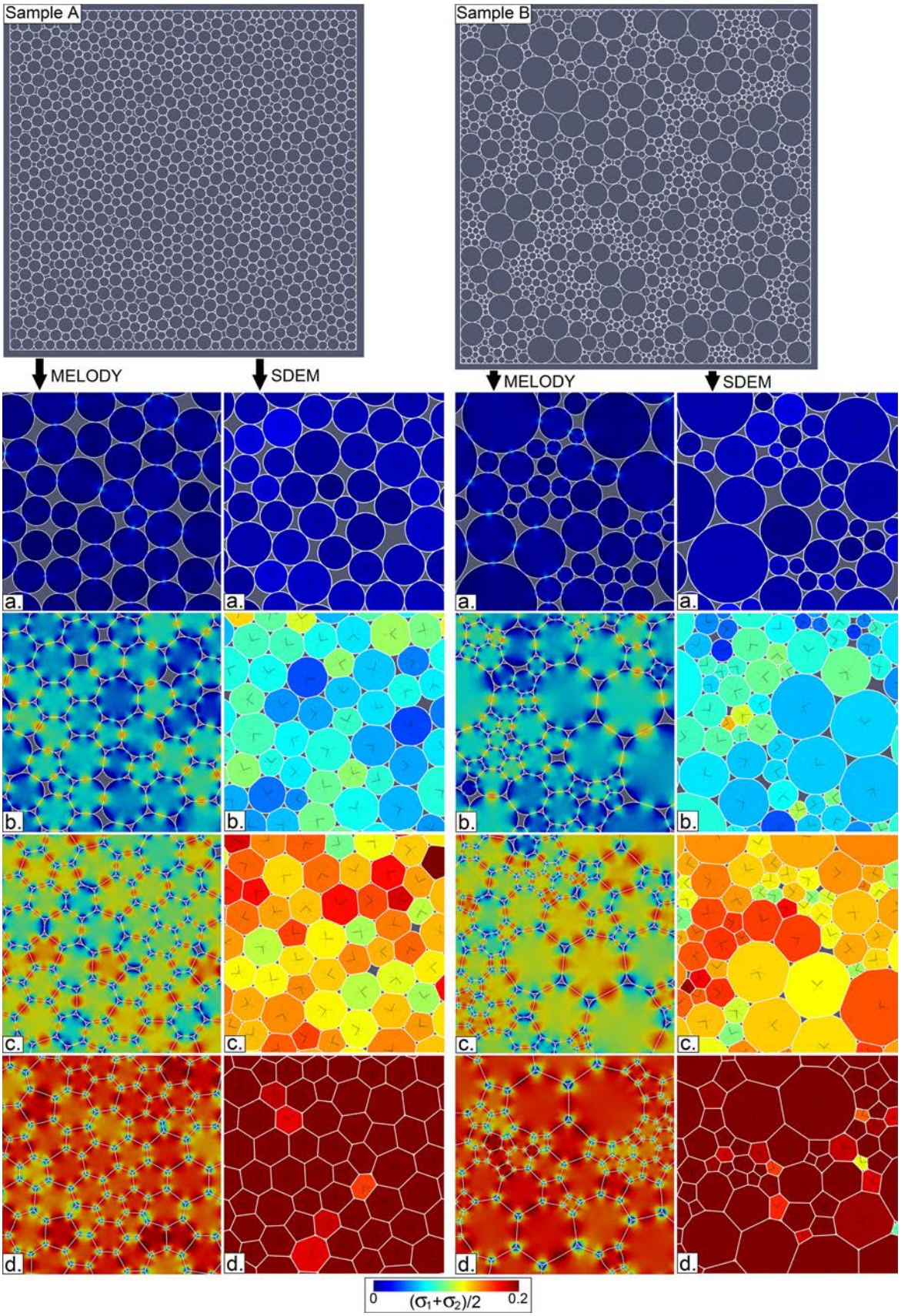
Sample A
Sample B
MELODY
SDEM
MELODY
SDEM
a.
b.
c.
d.
0
(σ1+σ2)/2
0.2

◂**Fig. 9** Zoomed views on isotropic compression tests as performed on samples A and B by MELODY (Multibody Meshfree Approach) and SDEM for $\nu = 0.3$. Loading stages **a** to **d** correspond to marks in Fig. 10

a rather narrow Gaussian size distribution, with an average radius of 0.012, a standard deviation of 0.0024 (coefficient of variation of 0.2), and lower and upper size cut-offs at 0.008 and 0.016 respectively. The sample B follows a fractal distribution of fractal dimension 2, with lower and upper cut-offs at 0.004 and 0.038 respectively. Both samples are frictionless, with a Young's modulus equal to 1, and a unit density. They are positioned between four rigid walls forming a unit square box and submitted to a strain-driven isotropic compaction in quasi-static conditions (i.e. at a slow enough pace to avoid any inertial effect).

It was recently shown in [33] that an analytical solution could be inferred for this kind of physical system in the case of incompressible grains. The mean stress in the sample was indeed reported to be well described by the following expression:

$$\sigma_n = -E \cdot \frac{b\phi}{2\pi} \cdot \left(Z_0 + k\left(\phi - \phi_0\right)^a\right) \cdot \ln\left(\frac{\phi_{\max} - \phi}{\phi_{\max} - \phi_0}\right) \quad (69)$$

In this expression, E is the Young's modulus of the grains, ϕ is the current solid fraction, Z_0 and ϕ_0 are the coordination number and the solid fraction at the jamming transition, and ϕ_{max} is the maximum solid fraction that can be attained in the sample (this value is reported to depend mostly on the friction coefficient between the grains, and is usually very close to 1). The pre-factor k and the exponent a are inherited from $Z - \phi$ relations reported in various studies [34–36] and take the values 5.1 and 0.5 respectively. The value of b was fitted in [33] based on single-grain compaction tests and is equal to 0.12.

Figure 8 shows a comparison between the $\sigma_n - \phi$ curves obtained with SDEM and with this analytical solution. For this comparison, the values of Z_0 and ϕ_0 are first measured at the jamming point for both samples (equal to 4.20 and 0.833 respectively for sample A, 4.22 and 0.858 respectively for sample B), and the value of ϕ_{max} is set to 1. The agreement between both approaches is very satisfactory.

To validate SDEM with different values of the Poisson's coefficient, however, a different approach must be used since the expression of Eq. (69) is only valid for $\nu = 0.5$. Simulations of isotropic compactions are thus performed on the same samples and in the same conditions with the code MELODY, using the Multibody Meshfree Approach. Qualitative results are provided in Fig. 9 for both samples, in the case $\nu = 0.3$. Four loading stages (provided in Fig. 10) are considered. Zoomed views on the same area of the sample are provided, and the grains are represented with a color scale corresponding to the local value of the mean stress $\left(\sigma_1 + \sigma_2\right)/2$. The agreement between both numerical approaches is acceptable, both in terms of mean stress values (although this quantity is constant in each grain for SDEM while it is allowed to vary spatially in MELODY thanks to a much finer discretization) and in grains motions and deformations. The progressive closure of the void space and the appearance of straight contact segments between grains at larger compaction is also well-rendered, even when the contacting grains have very different radii (Sample B). At loading stage d. (i.e. for a mean stress applied on the sample close to 0.3), the saturation of the sample is almost complete, and the stress level in the grains is slightly over-estimated by SDEM when compared with MELODY. This is probably related to the decrease in accuracy of the simple contact law calibrated in Fig. 7 when the interpenetration becomes too large. It may be corrected in future versions of the method with more accurate contact models.

Figure 10 covers the cases $\nu = 0.3$ and $\nu = 0.5$, and provides a quantitative view on this comparison. As shown in the upper part of the figure, SDEM is able to provide a good prediction of the compressibility of all samples, although this compressibility is slightly under-estimated at low pressures (i.e. $\sigma_n < 0.01$) and slightly over-estimated at large pressures (i.e. $\sigma_n > 0.1$). The lower part of the figure confirms that SDEM can also bring fair estimates of microstructural features of the samples, as it provides good first-order evaluations of the evolution of the coordination number $Z\left(\sigma_n\right)$ during compaction. The prediction of Z is especially good for $\nu = 0.3$, but a bit too large for low values of σ_n in the case of incompressible grains. It is interesting to notice that the quality of the SDEM approximation is not degraded by the presence of a very broad size distribution of the grains (Sample B).

5.2 Oedometric compression

In order to check the validity of SDEM under a less isotropic loading, samples A and B are submitted to an oedometric compression test. Starting from the isotropic jamming state, the right-hand wall is progressively moved leftwards in quasi-static conditions (i.e. slowly enough to avoid inertial effects in the samples). This operation is performed both with the SDEM and with the Multibody Meshfree Method in MELODY. The whole process is illustrated in Fig. 11 in the case of Sample B. SDEM and MELODY results are qualitatively very similar, and the magnitude of the mean stress inside the grains is well reproduced by SDEM.

During loading, with both approaches, we observe short events of reorganization of the samples, and the grains mostly keep a roughly circular shape (apart from the contact segments). We observe in Fig. 11e, h that some grains seem slightly elongated in the vertical direction, both with SDEM

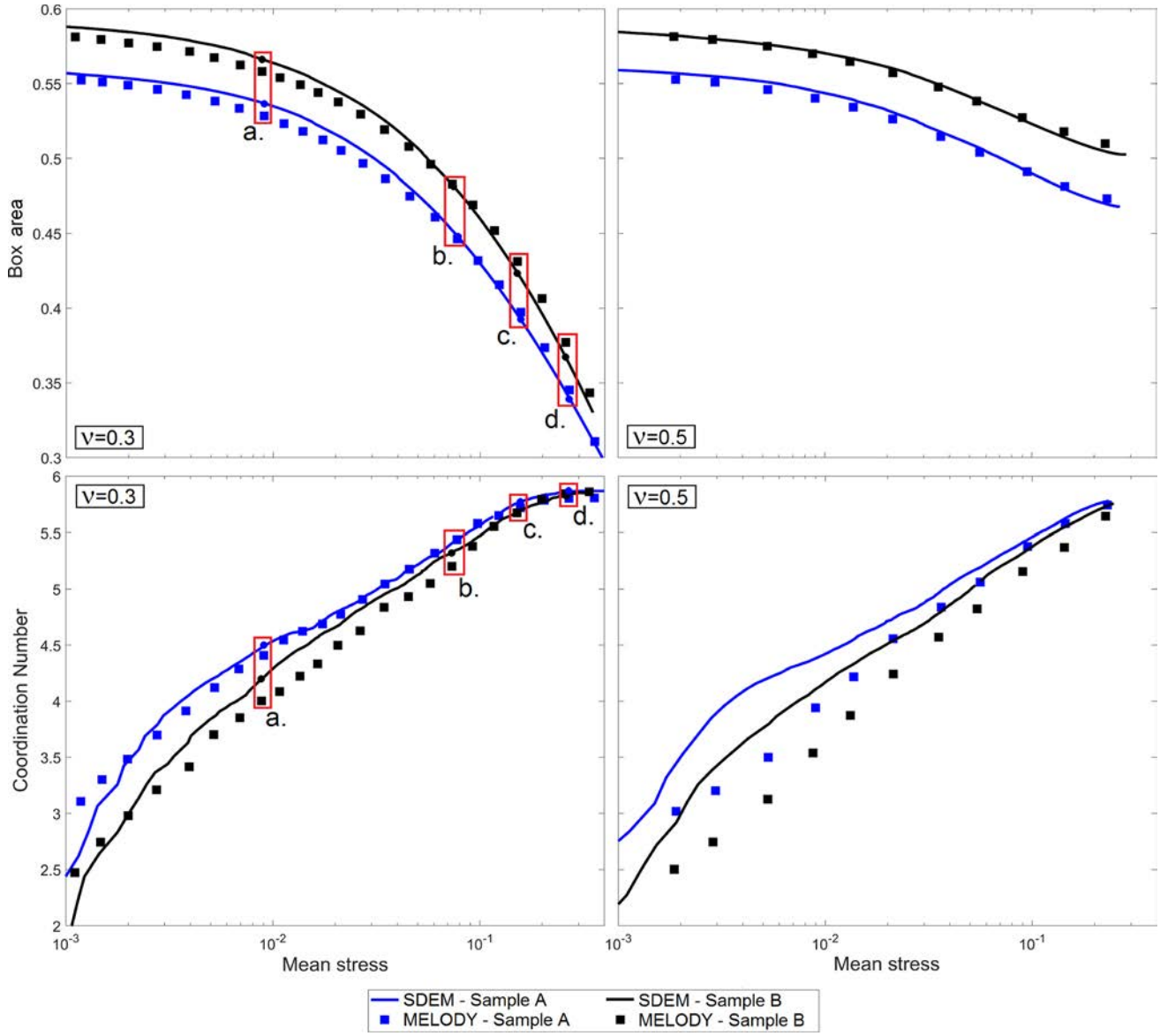

Fig. 10 Comparison with Multibody Meshfree Approach numerical solutions. Marks **a** to **d** are loading stages represented in Fig. 9

and MELODY, but this effect remains limited. Hence, despite the strongly deviatoric character of the loading path, the stress state in the sample does not seem to deviate much from a spherical stress state. This observation is to be attributed to the absence of friction and to the deformability of the grains. These properties simplify their relative motions and allow them to relax their internal stress field through simple changes in the granular configuration of the sample. It is likely that the presence of intergranular friction will lead the grains to adopt shapes more similar to those represented in Fig. 1b, although this will have to be confirmed when a more advanced version of the method includes this feature.

Figure 12 provides quantitative results provided by SDEM and MELODY during the simulations of samples A and B. The horizontal and vertical stresses σ_{xx} and σ_{yy} in the sample are computed based on the forces applied on the rigid walls. This figure shows that the increase of these stresses during loading and their stabilization at the end of the loading are well-reproduced by SDEM when compared to MELODY, with a relative error which remains below 10%. This figure also shows that the horizontal (in the direction of loading) and vertical (perpendicular to loading) stresses have the same order of magnitude at any loading state, but that the horizontal stress remains slightly larger than the vertical one. It means that both samples can develop a certain amount of deviatoric stress.

This is confirmed in Fig. 13, which plots the deviatoric stress $\left(\sigma_{xx} - \sigma_{yy}\right)/2$ against the mean stress $\left(\sigma_{xx} + \sigma_{yy}\right)/2$ in both samples, as predicted by SDEM and MELODY.

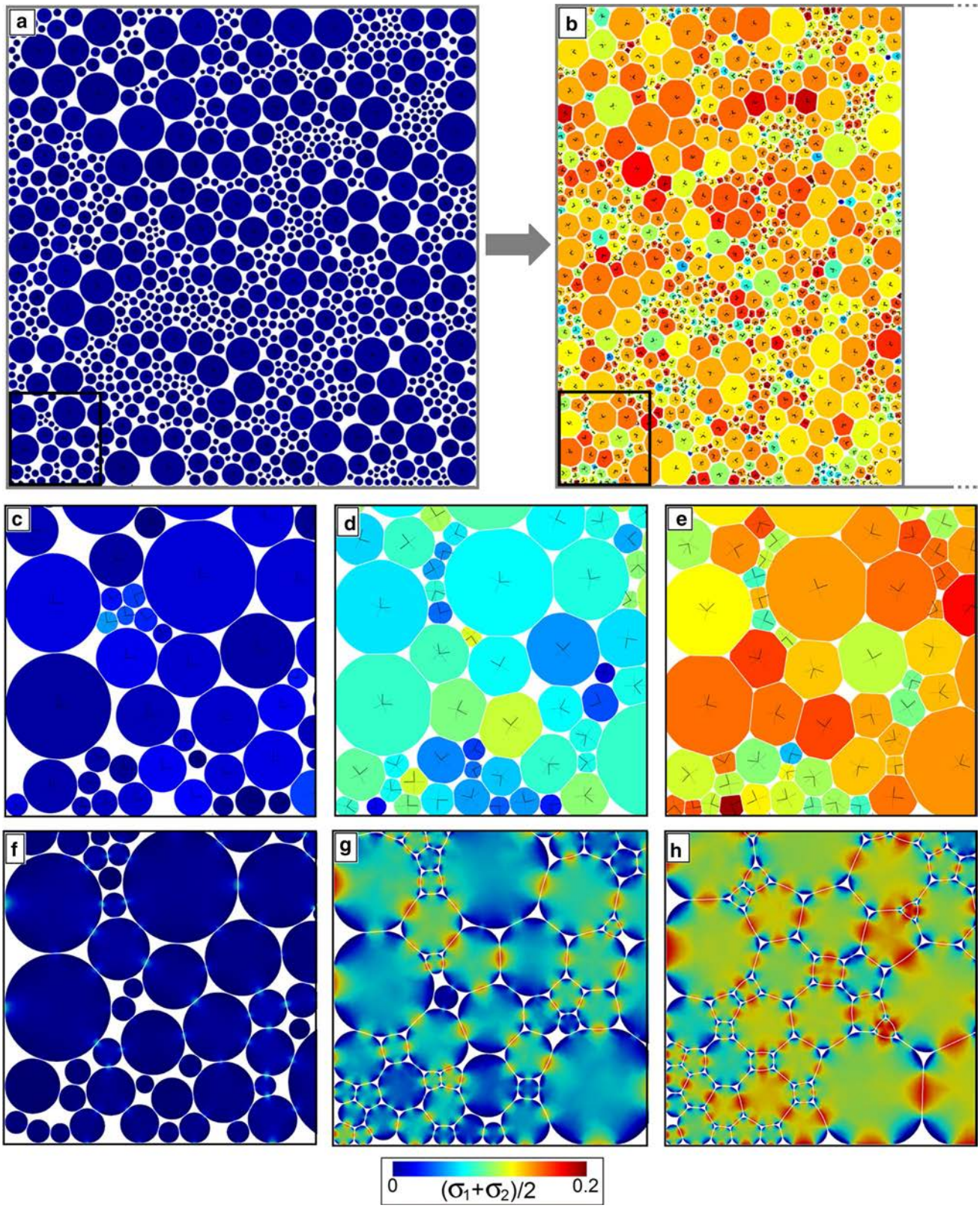

Fig. 11 Oedometric compression of sample B with SDEM: **a** Initial state (isotropic jamming point); **b** Final state; **c–e** Zoomed views (black square area in **a** and **b**) at t = 5, t = 15, and t = 25, respectively; **f–h** Same views of the same system simulated with MELODY

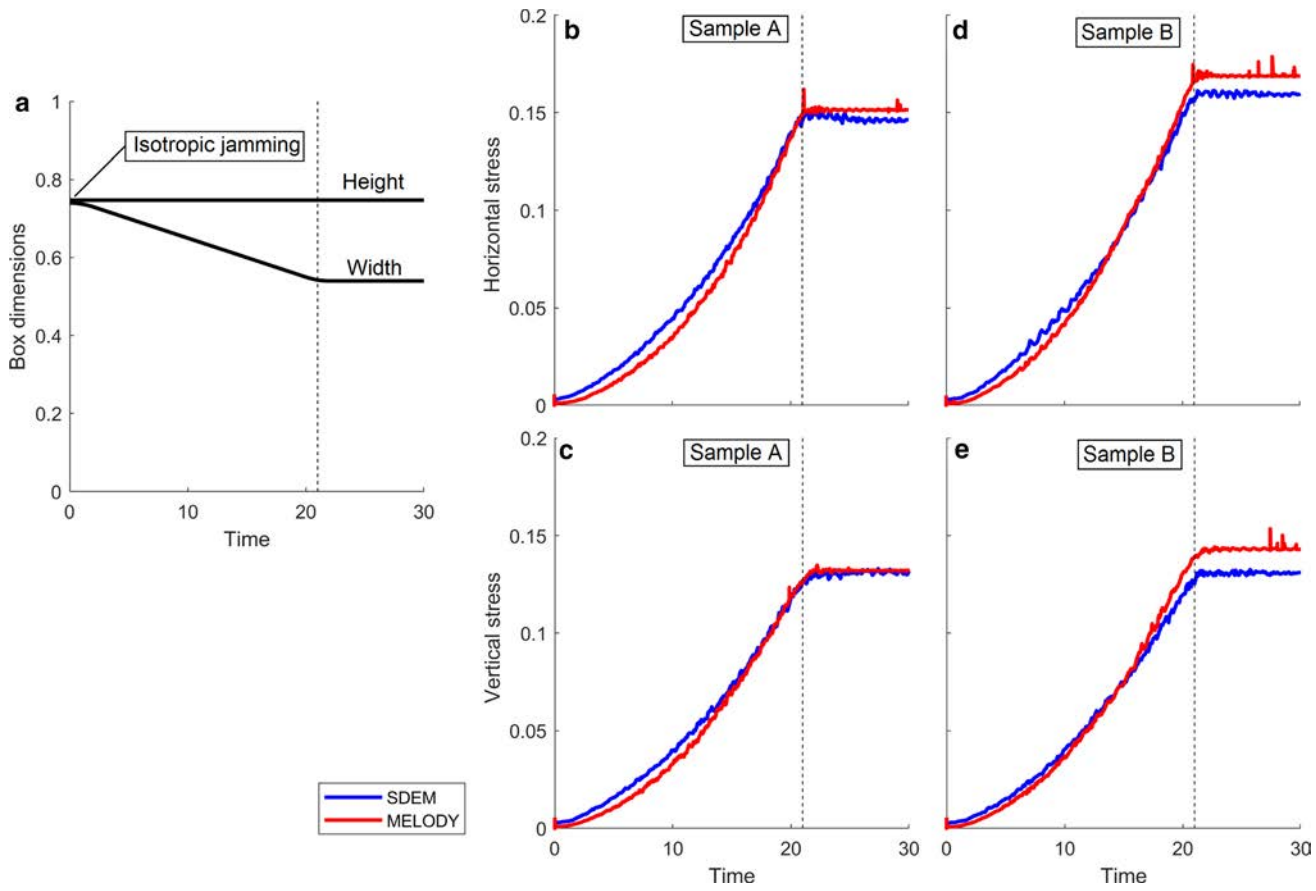

Fig. 12 Oedometric compression test results: **a** Strain-driven loading history; **b**, **c** Horizontal and vertical stresses in sample A; **d**, **e** Horizontal and vertical stresses in sample B

Data appear to be scattered, but some trends clearly appear. Both samples are able to develop a deviatoric stress, which increases with the mean stress. The relation between mean and deviatoric stress seems to follow a power law, although this would have to be confirmed by more careful and dedicated simulations. Both SDEM and MELODY predict that sample B presents a resistance to shearing slightly larger than sample A. In general, it appears that SDEM offers a satisfactory prediction of the oedometric response of soft granular samples, at least under the assumptions of the present study.

6 Conclusion and perspectives

The Soft Discrete Element Method introduced in this work is based on simplified kinematics of soft grains submitted to large contact forces. The main physical assumptions are a constant strain field within each grain (leading initially circular grains to deform into ellipses) and straight contact segments between contacting grains. To close the equations of motion corresponding to these kinematics, a simplistic

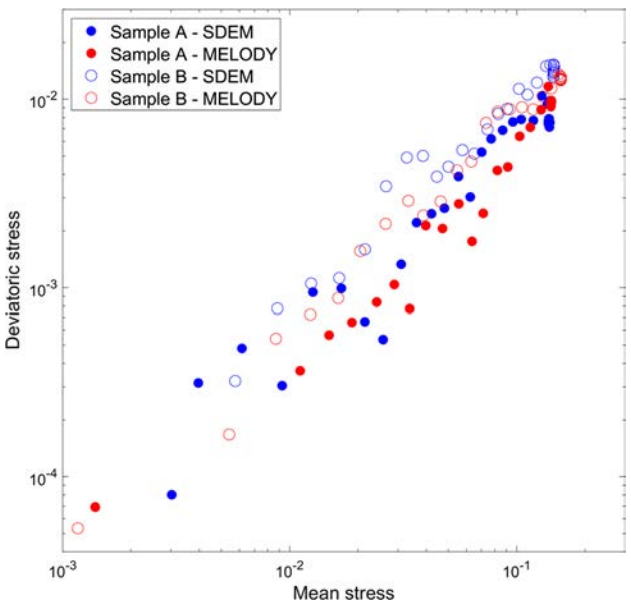

Fig. 13 Mean and deviatoric stresses in samples A and B as predicted by SDEM and MELODY

contact model is proposed in the frictionless case, based on simulations of single-grain compaction. The whole problem is integrated in time by an explicit solver, and solutions are proposed to ensure stability and incompressibility and to introduce damping. The general approach is successfully validated in the cases of isotropic and oedometric compactions, by comparison with an analytical formula and a more accurate numerical approach, for various Poisson's coefficients and grains size distributions.

The conceptual simplicity of this method might make it possible to implement it in existing DEM codes. The main interest of this novel technique when compared to the current state of the art in soft grains modelling lies in the computation time. If we consider a single grain, a reasonable discretization in the Multibody Meshfree Framework requires about 100–150 field nodes, which corresponds to 200–300 degrees of freedom. The critical time step in such a system is driven by the nodes located at the boundaries of the grains, which are characterized by a low mass (because discretization is generally refined in the vicinity of the grains contour) and large stiffness (because the non-interpenetration condition with any contacting body requires a large contact stiffness). It is therefore necessary to adopt very low time steps to ensure stability of the solver. On the other hand, the Soft Discrete Element Method only considers six degrees of freedom per grain, and can be integrated in time with much larger time steps since the contact stiffness is comparatively rather low (Eq. 57). After implementation in an efficient and optimized code, CPU costs are thus expected to drop by 2 to 4 orders of magnitude when using SDEM instead of more finely discretized techniques. Obviously, this gain comes at the expense of a reduced accuracy at the local scale and of a questionable relevance in fully dynamic conditions.

A basic version of the method was presented in this paper, but it is important to stress that this framework is particularly versatile. Future extensions of SDEM may indeed include more complex constitutive behaviours for the grains deformability (such as hyperelasticity, plasticity, etc.) and more complex contact models (friction, cohesion, capillary adhesion, etc.). Kinematics could be either enriched or degraded: if we call the present approach the D2F3-SDEM (2 dimensions, 3 DoF in deformation), standard DEM might then be called D2F0-SDEM. Other versions such as D2F1-SDEM (volumetric deformation only) or D3F6-SDEM could be imagined. A 3D extension seems indeed possible, since the computation of stress and strains tensors will be straightforward. It will however require specific algorithms for rapid computation of large interpenetrations between ellipsoids, and a calibration of contact laws with an accurate 3D code including contacts, in the manner of Fig. 7. A natural and simple extension would also consist in considering ellipses instead of discs, i.e. to modify the elastic state of reference for each body. With such features, SDEM can be expected to have an interesting potential for upscaling simulations of soft grains samples in granular science, complex fluids rheology, soft matter physics, geophysics, and tribology.

Acknowledgements The authors acknowledge that this study contains original material, as a result of a purely academic study without any kind of private funding or conflict of interest. Its publication has been approved tacitly by the responsible authorities at the institutes where the work has been carried out.

Declarations

Conflict of interest The authors declare that they have no conflict of interest.

References

1. Cundall, P.A., Strack, O.D.L.: A discrete numerical model for granular assemblies. Géotechnique **29**(1), 47–65 (1979)
2. Mollon, G., Zhao, J.: 3D generation of realistic granular samples based on random fields theory and Fourier shape descriptors. Comput. Methods Appl. Mech. Eng. **279**, 46–65 (2014)
3. Mollon, G., Richefeu, V., Villard, P., Daudon, D.: Discrete modelling of rock avalanches: sensitivity to block and slope geometries. Granular Matter **17**(5), 645–666 (2015)
4. Mollon, G., Quacquarelli, A., Andò, E., Viggiani, G.: Can friction replace roughness in the numerical simulation of granular materials? Granular Matter **22**, 42 (2020)
5. Scholtès, L., Hicher, P.Y., Nicot, F., Chareyre, B., Darve, F.: On the capillary stress tensor in wet granular materials. Int. J. Numer. Anal. Methods Geomech. **33**(10), 1289–1313 (2011)
6. Luding, S.: Cohesive, frictional powders: contact modes for tension. Granular Matter **10**, 235–246 (2008)
7. Tran, D.K., Prime, N., Froiio, F., Callari, C., Vincens, E.: Numerical modelling of backward front propagation in piping erosion by DEM-LBM coupling. Eur. J. Environ. Civil Eng. **21**(7–8), 960–987 (2017)
8. Renouf, M., Fillot, N.: Coupling electrical and mechanical effects in discrete element simulations. Int. J. Numer. Methods Eng. **74**, 238–254 (2008)
9. Gethin, D.T., Lewis, R.W., Ransing, R.S.: A discrete deformable element approach for the compaction of powder systems. Model. Simul. Mater. Sci. Eng. **11**, 101–114 (2003)
10. Güner, F., Necati Cora, Ö., Sofuoglu, H.: Numerical modeling of cold powder compaction using multi particle and continuum media approaches. Powder Technol. **271**, 238–247 (2015)
11. Nguyen, T.H., Nezamabadi, S., Delenne, J.Y., Radjai, F.: Compaction of granular materials composed of deformable particles. In: Powders and Grains 2017, EPJ Web of Conferences, vol 140, p 05013 (2017)
12. Boromand, A., Signoriello, A., Ye, F., O'Hem, C.S., Shattuck, M.D.: Jamming of deformable polygons. Phys. Rev. Lett. **21**, 248003 (2018)
13. Mollon, G.: A multibody meshfree strategy for the simulation of highly deformable granular materials. Int. J. Numer. Methods Eng. **108**(12), 1477–1497 (2016)
14. Mollon, G.: A unified numerical framework for rigid and compliant granular materials. Comput. Part. Mech. **5**(4), 517–527 (2018)
15. Mollon, G.: MELODY 2D. (2020)
16. Mollon, G.: Mixture of hard and soft grains: micromechanical behavior at large strains. Granular Matter **20**(3), 1–16 (2018)

17. Mollon, G.: Solid flow regimes within dry sliding contacts. Tribol. Lett. **67**, 120 (2019)
18. Zhang, Y., Mollon, G., Descartes, S.: Significance of third body rheology in friction at a dry sliding interface observed by a multi-body meshfree model: influence of cohesion between particles. Tribol. Int. **145**, 106188 (2020)
19. Mollon, G., Aubry, J., Schubnel, A.: Simulating melting in 2D seismic fault gouge. J. Geophys. Res. Solid Earth **126**, e2020JB021485 (2021)
20. Chinesta, F., Ladeveze, P., Cueto, E.: A short review on model order reduction based on proper generalized decomposition. Arch. Comput. Methods Eng. **18**, 395 (2011)
21. Amsallem, D., Zahr, M.J., Farhat, C.: Nonlinear model order reduction based on local reduced-order bases. Int. J. Numer. Methods Eng. **92**(10), 891–916 (2012)
22. Corigliano, A., Dossi, M., Mariani, S.: Model Order Reduction and domain decomposition strategies for the solution of the dynamic elastic-plastic structural problem. Comput. Methods Appl. Mech. Eng. **290**, 127–155 (2015)
23. Popov, V.L., Psakhie, S.G.: Theoretical principles ofmodeling elastoplastic media by movable cellular automata method. I. Homogeneous media. Phys. Mesomech. **4**(1), 15–25 (2001)
24. Salman, N., Wilson, M., Neville, A., Smolin, A.: Implementation of MCA in the framework of LIGGGHTS. In: Proceedings of the 5th International Conference on Particle-Based Methods - Fundamentals and Applications (PARTICLES 2017). PARTICLES 2017, 26–28 Sep 2017, Hannover, Germany. International Center for Numerical Methods in Engineering (CIMNE) (2017), pp. 767–777. ISBN 9788494690976
25. Hertz, H.: Uber die Beruhrung fester elastischer Korper. J. Reine Angew. Math. **92**, 156–171 (1881)
26. Mindlin, R.D.: Compliance of elastic bodies in contact. J. Appl. Mech. **16**, 259–268 (1949)
27. Nicot, F., Hadda, N., Guessasma, M., Fortin, J., Millet, O.: On the definition of the stress tensor in granular media. Int. J. Solids Struct. **50**, 2508–2517 (2013)
28. Rothenburg, L., Bathurst, R.J.: Numerical simulation of idealized granular assemblies with plane elliptical particles. Comput. Geotech. **11**, 315–329 (1991)
29. Ting, J.M.: A robust algorithm for ellipse-based discrete element modelling of granular materials. Comput. Geotech. **13**, 175–186 (1992)
30. Ting, J.M., Khwaja, M., Meachum, L.R., Rowell, J.: An ellipse-based discrete element model for granular materials. Int. J. Numer. Anal. Methods Geomech. **17**(9), 603–623 (1993)
31. Gu, X., Yang, J., Huang, M.: DEM simulations of the small strain stiffness of granular soils: effect of stress ratio. Granular Matter **15**, 287–298 (2013)
32. Richefeu, V., Mollon, G., Daudon, D., Villard, P.: Dissipative contacts and realistic block shapes for modeling rock avalanches. Eng. Geol. **149**, 78–92 (2012)
33. Cantor, D., Cardenas-Barrantes, M., Preechawuttipong, I., Renouf, M., Azéma, E.: Compaction model for highly deformable particle assemblies. Phys. Rev. Lett. **124**, 208003 (2020)
34. Andreotti, B., Forterre, Y., Pouliquen, O.: Granular media, between fluid and solid. Cambridge University Press, Cambridge, England (2013)
35. Vu, T.L., Barès, J., Mora, S., Nezamabadi, S.: Numerical simulations of the compaction of assemblies of rubberlike particles: a quantitative comparison with experiments. Phys. Rev. E **99**, 062903 (2019)
36. Nezamabadi, S., Franck, X., Delenne, J.Y., Averseng, J., Radjai, F.: Parallel implicit contact algorithm for soft particle systems. Comput. Phys. Commun. **237**, 17–25 (2019)